Journal of Trace Elements in Medicine and Biology 51 (2019) 212–218

Contents lists available at ScienceDirect

Journal of Trace Elements in Medicine and Biology

journal homepage: www.elsevier.com/locate/jtemb

Analytical methodology

LA-ICP-MS/MS improves limits of detection in elemental bioimaging of gadolinium deposition originating from MRI contrast agents in skin and brain tissues

David Clases[a,b], Stefanie Fingerhut[a], Astrid Jeibmann[c], Michael Sperling[a,d], Philip Doble[b], Uwe Karst[a,*]

[a] University of Münster, Institute of Inorganic and Analytical Chemistry, Corrensstr. 30, 48149, Münster, Germany
[b] Elemental Bioimaging Facility, University of Technology Sydney, Broadway, 2007, NSW, Australia
[c] University Hospital Münster, Institute of Neuropathology, Pottkamp 2, 48149, Münster, Germany
[d] European Virtual Institute for Speciation Analysis (EVISA), Mendelstraße 11, 48149, Münster, Germany

ARTICLE INFO

Keywords:
Gadolinium retention
NSF
LA-ICP-MS
ICP-MS/MS
Quantitative bioimaging

ABSTRACT

A novel analytical method to detect the retention of gadolinium from contrast agents for magnetic resonance imaging (MRI) in tissue samples of patients is presented. It is based on laser ablation - inductively coupled plasma - triple quadrupole - mass spectrometry (LA-ICP-MS/MS). Both Gd and P were monitored with a mass shift of +16, corresponding to mono-oxygenated species, as well as Zn, Ca, and Fe on-mass. This method resulted in a significantly reduced background and improved limits of detection not only for phosphorus, but also for gadolinium. These improvements were essential to perform elemental bioimaging with improved resolution of 5 µm x 5 µm, allowing the detection of small Gd deposits in fibrotic skin and brain tumour tissue with diameters of approximately 50 µm. Detailed analyses of these regions revealed that most Gd was accompanied with P and Ca, indicating co-precipitation.

1. Introduction

The deposition of Gd originating from Gd-based contrast agents (GBCAs) in biological tissue has caused major concerns in the past decade. Grobner et al. first identified that Gd may be retained inside the body and may lead to a potentially fatal disease known as nephrogenic systemic fibrosis (NSF) [1]. NSF was first observed in patients with impaired renal function [2,3]. It took a further six years for the correlation of the development of NSF with the administration of GBCAs for magnetic resonance imaging (MRI) examinations conducted several years before [4]. Pathologies such as diffuse ulcerative calcific atherosclerosis, patchy myocardial necrosis, fibrosis and necrotic skin were also identified in patients with MRI history without renal dysfunction [5]. Kasahara et al. reported that Gd can be found in the dentate nucleus of MRI patients with a history of brain irradiation [6]. Xia et al. also identified Gd deposits in brain tumour samples obtained from five MRI patients without renal dysfunction by energy dispersive X-ray spectroscopy (SEM/EDS), and demonstrated that the deposits also contained Ca and P [7]. Ever since a FDA safety announcement in 2015 [8], the retention of Gd has attracted more concerns and triggered further investigations which were reviewed recently [9].

The development of NSF appears to be highly dependent on the type of the GBCA administered as different forms have disparate retention of Gd in the brain and other organs. Nevertheless, Gd retention in NSF and brain tissues has been reported for all categories (ionic/non-ionic, linear/macrocyclic) of GBCAs. Non-ionic, linear GBCAs have been identified as the most problematic [10–13]. Birka et al. were able to show the presence of intact GBCAs in NSF skin biopsies of a patient by hydrophilic interaction liquid chromatography (HILIC) coupled to ICP-MS, as well as confirm the deposition and accumulation of Gd with Ca and P in NSF tissues by laser ablation-inductively coupled plasma-mass spectrometry (LA-ICP-MS) [14]. These results were subsequently confirmed by Roberts et al. [15].

Recently, Fingerhut et al. demonstrated the retention of Gd in specific brain regions of humans treated with GBCAs and located Gd in distinct cell types within these regions [16,17]. The pathogenesis of NSF as well as the mechanism of retention of Gd in specific brain regions such as the dentate nucleus still is largely unknown. Although GBCAs are considered to be thermodynamically stable and kinetically inert, it is hypothesised that Gd is released and precipitates, possibly together with calcium as (mixed) phosphate. Transmetallation reactions are suspected to play a crucial role for the

* Corresponding author.
E-mail address: uk@uni-muenster.de (U. Karst).

https://doi.org/10.1016/j.jtemb.2018.10.021
Received 25 June 2018; Received in revised form 18 September 2018; Accepted 29 October 2018

release of Gd [5,18], as well as metabolism and elimination of GBCAs, which is compromised in patients with renal dysfunction [19]. The formation of small deposits of Gd and coprecipitation with Ca and P within various organs has been observed with imaging techniques such as element specific transmission electron microscopy (TEM), scanning electron microscopy/energy dispersive X-ray spectroscopy (SEM/EDX), secondary ion mass spectrometry (SIMS), synchrotron X-ray fluorescence (SXRF) and extended X-ray absorption fine structure (EXAFS) spectroscopy [7,19–27]. However, the relationship of these deposits and the pathogenesis of NSF has not been fully explored. One hypothesis is that circulating fibrocytes respond to the deposits to initiate fibrosis [28].

Accordingly, the investigation of the mechanism of NSF progression in relation to Gd deposits with diameters of approximately 50 µm requires a method that is capable of quantitative imaging with high spatial resolution and low limits of detection. Triple quadrupole technology for ICP-MS enhances the analysis of many elements by performing tandem mass spectrometry and was first hyphenated to a LA system in 2016 for elemental bioimaging [29]. Tandem mass spectrometry for ICP-MS has enhanced detection capabilities for many elements to improve detection limits and remove potential interferences. One approach to avoid spectral interferences is by shifting the analytes' mass with favoured chemical reactions in the collision/reaction cell by adding a dedicated reaction gas. The selection of the reaction gas, the reaction conditions and the impact on the analysis must be evaluated carefully. Bolea-Fernandez et al. and Balcaen et al reviewed the theoretical background and recent applications, methods, theory and instrumentation [30,31].

In this work, we present a new method for the investigation of Gd deposition in a NSF skin sample as well as in a cancerous brain sample of a MRT patient by LA-ICP-MS/MS. The limits of detection (LOD) for trace elements believed to play a key role in NSF, such as Gd, P, Ca, Fe and Zn, were compared against single quadrupole LA-ICP-MS to demonstrate the advantages of the LA-ICP-MS/MS method.

2. Experimental

2.1. Sample preparation

For elemental bioimaging (EBI), NSF samples were obtained from the "*Johannes Wesling Klinikum*" (hospital) in Minden in April 2013 and originate from a 25-year-old female patient. A biopsy of an affected skin area was taken and immediately frozen to -20 °C. The patient showed typical NSF symptoms including swollen and sclerotic skin. The clinical history included a kidney transplantation and on-going impaired renal function requiring regular dialysis. The patient underwent MRI examinations with the linear GBCA gadopentetate (Gd-DTPA, Bayer Vital (Leverkusen, Germany)) in 2002, and with the macrocyclic GBCA gadoteridol (Gd-HP-DO3A, Bracco Imaging, 0.5 M (Konstanz, Germany)) in 2005. The first symptoms appeared two years prior to the skin biopsy. For analysis, the skin sample was cut axially to 20 µm thickness using a cryotome (CryoStat™ NX70, Thermo Fisher Scientific) at 30 °C and placed onto glass slides. For a histological grading, a sequential slide was stained with hematoxylin and eosin (H&E) to visualise tissue structures.

Brain tumour samples were obtained from the archives of the Institute of Neuropathology, University Hospital Münster and originated from a female 77 years old patient who was suffering from a glioblastoma, IDH wild type (grade IV WHO). She underwent an MRI examination with 20 mL of Gd-HP-DO3A. Samples were collected eleven days after the MRI examination during a biopsy and immediately frozen to −20 °C, cut to a thickness of 20 µm and mounted onto glass slides.

For both patients, it should be noted that it cannot be excluded that they received Gd-based contrast agents prior to the treatment period which is documented above. Therefore, the Gd deposition detected in this work cannot be unambiguously traced back to the contrast agents, which are known to have been administered.

Table 1
Concentration levels of P, Ca, Fe, Zn and Gd present in the (matrix-matched) standards used for the generation of calibration curves and the subsequent determination of LODs. *In case of P, diluted standard solutions instead of spiked matrix samples were used for calibration.

Level	P* [ng/g]	Ca [µg/g]	Fe [µg/g]	Zn [µg/g]	Gd [µg/g]
1	0	37.7	15.3	11.3	0.00
2	0.001	43.0	16.5	11.4	0.21
3	0.01	48.7	19.0	14.9	2.21
4	1	64.1	37.5	24.0	10.6
5	10	86.4	59.8	36.1	21.1

2.2. Calibration strategy

Quantification of Gd and the determination of LODs of the elements of interest were performed by in-house prepared matrix-matched standards consisting of homogenised lamb brain spiked with respective elements and mounted in thin tissue sections with a thickness of 20 µm on glass slides. A detailed procedure for the fabrication, storage, quality control as well as the data analysis was already reported earlier by Hare et al. [32]. The matrix-matched standards were counter-quantified after digestion with 1 mL 30–32% H_2O_2 and 4 mL 70% HNO_3 (Seastar Baseline, Choice Analytical, Galveston, USA) using conventional liquid sample introduction with a 7500cx ICP-MS system (Agilent Technologies, Mulgrave, Victoria, Australia), shown in Table 1. The accuracy of the approach was validated using a BCR185R bovine liver reference standard.

2.3. Instrumentation and tune development

For EBI, elements of interest were analysed with individual integration times on a 8800 series ICP-MS/MS system (Agilent Technologies, Mulgrave, Victoria, Australia) coupled to a New Wave Research NWR193 laser ablation unit (Kennelec Scientific, Mitcham, Victoria, Australia). ($^{31}P/^{31}P^{16}O$: 50 ms, ^{44}Ca: 40ms, ^{57}Fe: 35 ms, ^{64}Zn: 35 ms, $^{158}Gd/^{158}Gd^{16}O$, 47 ms). The single quadrupole (SQ) tune was developed according to Lear et al. [33]. The laser scan speed and the spot size of the ArF excimer laser emitting nanosecond laser pulses at 193 nm were adapted to generate squared pixels. For preliminary scans and comparison of LA-ICP-MS/MS against the LA-ICP-SQ-MS tunes, 50 µm laser beam spot size and 200 µm/s scan speed were chosen. For the high-resolution images, the parameters were adjusted to 5 µm and 20 µm/s, respectively. The sensitivity of the ICP-MS system was monitored on a daily basis and optimised with a tune solution containing ^{7}Li, ^{89}Y and ^{205}Tl. A low oxide formation was guaranteed by monitoring the ThO/Th ratio (< 0.3%) and the P/A factor was adjusted before each measurement. For the MS/MS tune development, the ICP-MS/MS system was equipped with a MicroMist concentric nebuliser (Elemental Scientific, Omaha, NE, USA) and a Scott-type double-pass spray chamber (Glass Expansion, West Melbourne, Victoria, Australia). Using this liquid sample introduction system arrangement, plasma independent parameters were optimised to achieve lower LODs. Finally, dry plasma conditions were adapted for the operation of LA-ICP-MS. The initial tuning was performed by ablation of a NIST 612 "Trace Element in Glass" certified reference material (CRM), whereas the fine tuning was performed by monitoring the m/z of interest during the ablation of matrix-matched standards. The optimised tune parameters were: cell entrance, -75 V; OctP RF, 180 V; OctP bias, -5 V; deflect, 5 V; energy discrimination, 8 V; O_2 cell gas flow, 0.32 mL/min; waiting time offset, 8 ms. To avoid long settling times caused by multiple filling and evacuation of the collision/reaction cell, all elements of interest were analysed with oxygen present as reaction gas. However, only P and Gd were monitored with a + 16 amu mass shift. In SQ mode, the first quadrupole was used as a band-pass filter and the ICP-MS/MS system provided the best figures of merit for all analytes when operating the

collision/reaction cell with H_2 gas flow of 3 mL/min [33]. To compare the figures of merit of both tunes, LODs were calculated based on the 3σ criterion by ablating line scans on matrix-matched tissue sections with a laser spot size of 50 µm and a scan speed of 200 µm/s. The standard deviation was derived from the shutter blank and the respective sensitivities from five-point calibration curves. In the case of P, the natural background and the variations in matrix-matched tissue derived from living organisms were too high for the estimation of the benefits of ICP-MS/MS over ICP-SQ-MS. Therefore, generation of a calibration curve for the determination of the LODs was conducted with diluted standard solutions on a liquid sample introduction system as described previously to demonstrate the advantages of the MS/MS tune. Quantification of high resolution data obtained using a laser beam spot size of 5 µm was solely conducted for Gd. A calibration curve was generated considering the standard deviations of each calibration point. The deviations were weighted according to Eq. (1). The deviation of 0 cps at a Gd concentration of 0 µg/g was weighted with 1.

$$\omega = \frac{1}{\sigma^2} \tag{1}$$

Where, ω is the weighting factor and σ is the standard deviation. The ICP-MS/MS system was operated with MassHunter software (Agilent Technologies). The LA unit was operated with ActiveView software (Electro Scientific Industries, Portland, Oregon, USA). The analytical figures of merit were processed using Origin software version 9 (OriginLab Corporation, Northhampton, MA, USA). Element images were generated using MassImager 3.17 software, an in-house developed program for image visualisation.

3. Results and discussion

3.1. Tune development for EBI

On-mass or mass-shift MS/MS detection requires consideration of the reaction enthalpies. Both P and Gd have negative reaction enthalpies with O_2 and were amenable for mass-shift monitoring at +16 amu. The remaining target elements Ca, Fe and Zn were monitored on-mass. Oxygen acted here as both reaction and collision gas. For the oxophilic elements P and Gd, mass shifting and tandem mass spectrometry resulted in a reduced background and therefore overall improved signal to noise ratios. The elements Ca, Zn and Fe showed improved figures of merit when analysed on-mass due to the collisional elimination of polyatomic interferents. The benefits of such detection modes for the elements were demonstrated via comparison of LODs against a standard ICP-SQ-MS method. The LODs were estimated by construction of calibration curves by LA line scans (50 µm spot size) of the matrix matched standards and application of the 3σ criterion or by estimation of the minimal detectable concentration (Fig. 1). In case of P, the determination of the LODs was performed via liquid standards as the matrix matched tissue standards had high backgrounds and variable content.

Due to highly abundant isobaric polyatomic interferents in the low mass range, the MS/MS tune for P resulted in a crucial improvement of 16.2fold lower LODs. In case of Gd, the MS/MS tune eliminated the background to 0 cps, precluding the calculation of the LOD with the 3σ criterion. Instead, we used the lowest concentration (1.1 ng/g) that provided the least measurable signal (21 counts/s). This value was a 5.5-fold improvement compared against the ICP-SQ mode. For Fe, Ca and Zn, the ICP-MS/MS improvement factors were 28.3, 31.8, and 3.6, respectively.

These improved LODs of the ICP-MS/MS were essential to successfully image, characterise and quantify the Gd deposits at higher resolutions of 5 µm. The LODs for Gd obtained by the 5 µm LA-ICP-MS/MS tune was 48 ng/g.

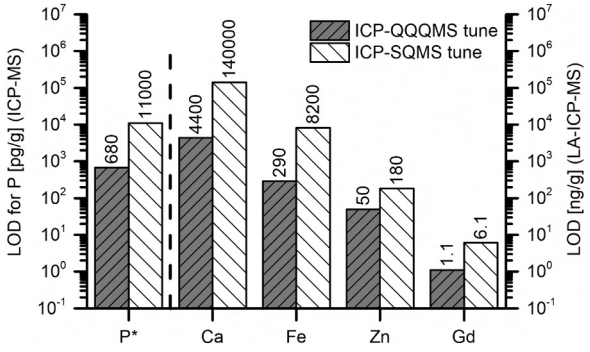

Fig. 1. Comparison of LODs obtained by (LA-)ICP-MS/MS and (LA-)ICP-SQ-MS. *In case of P, LODs were determined using a calibration curve obtained from diluted standards introduced via a liquid sample introduction system whereas the LODs of Gd, Fe, Ca and Zn originate from the dry plasma MS/MS tune performed in line-by-line scans on matrix-matched standards by LA-ICP-MS/MS.

3.2. NSF skin samples

The large dimensions of the sample (approximately 3 cm x 0.8 cm) spanning various anatomical structures required a low resolution preliminary scan (pixel dimensions: 50 µm x 50 µm) to disclose regions of interest with dense distributions of Gd deposits. Fig. 2 shows the quantitative distribution of Gd in the NSF skin sample and the corresponding microscopic image.

Although there were hot spots of Gd deposits located throughout the sample (Fig. 2), there were three areas of obvious accumulation, labelled (a), (b) and (c). Region of interest (a) had the most dense distribution of pixels with concentrations calculated via extrapolation to exceed 100 µg/g. Regions (b) and (c) consisted of a blood vessel and connective tissue, respectively, and had concentrations also exceeding 100 µg/g. Area (a) was targeted for further investigation with a higher resolution of 5 µm.

Various layers of the skin within the region of interest were identified by a haematoxylin and eosin (H&E) stain of a consecutive section, which is shown in Fig. 3. The epidermis is visible at (d), and fibrotic tissue at location (e) can be seen intermingled with fatty tissue areas (f). These histological findings are similar to those as described by Schäd et al. [21].

A high-resolution (5 µm x 5 µm) LA-ICP-MS image of Gd, P, Ca, Fe and Zn, and a light photomicrograph of area (a) are shown in Fig. 4. The improved resolution revealed hotspots of all target elements within small deposits of approximately 50 µm in the fibrotic tissue. The elemental distribution of Gd, P, Ca and Zn correlated in location and shape clearly demonstrating the abundance of insoluble phosphate species. Correlations with Fe were not observed. These observations were consistent with other investigations by SIMS [22], SXRF and EXAFS [20]. Smaller deposits were reported by Thakral et al. using TEM [19].

Fig. 5 presents a zoom view of area (a) to further visualise the composition of the deposits. Most of the Gd throughout the specimen was located within the deposits with the highest concentrations in the centre exceeding 100 µg/g. An overlay of Gd (green) and P (red) clearly shows co-localisation within the deposits. Similar correlations were found in accumulations for Ca and Zn. The most likely explanation for this distribution is the co-precipitation of Gd with calcium and zinc phosphate, when the concentration of the circulating free Gd and phosphate ions exceeds the solubility limits of Gd-phosphate (pK_{SP} = 25.39). Only the core of the deposits is made of Gd whereas the shell seems to have an increasing fraction of P. This indicates that the Gd phosphate deposits may function as nucleation centre favouring the subsequent growth.

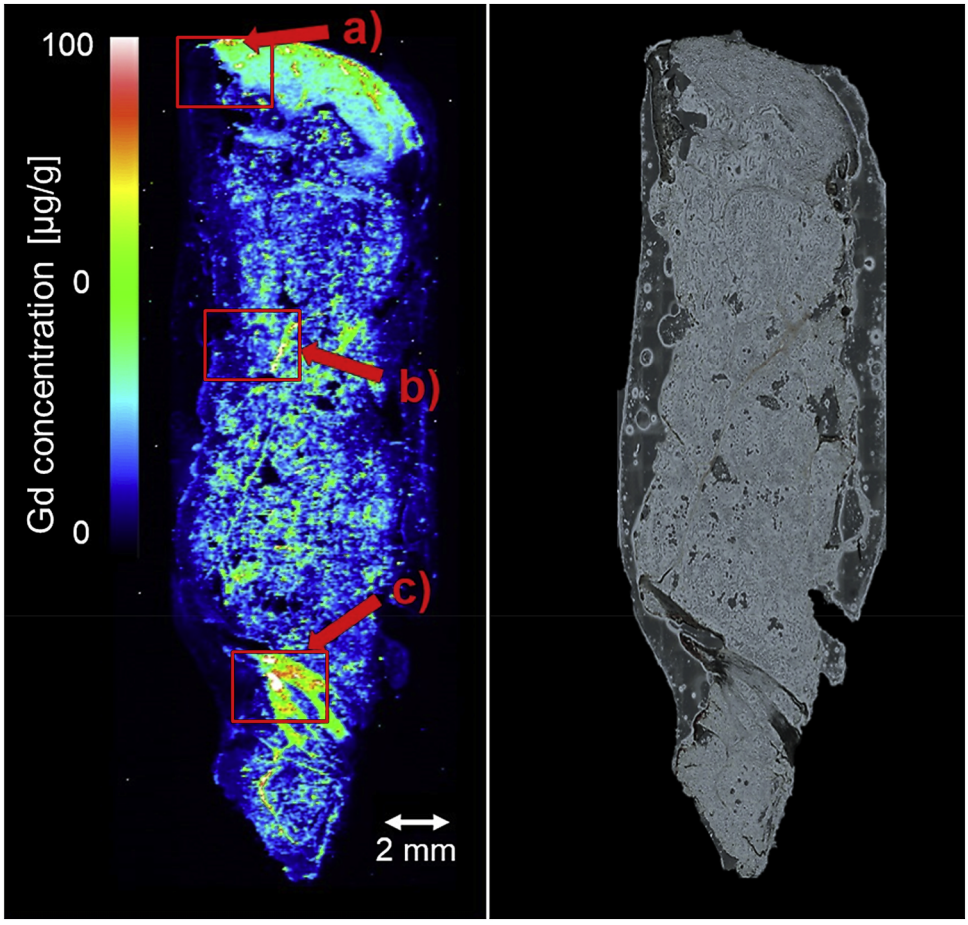

Fig. 2. Comparison of the elemental Gd distribution and the corresponding microscopic image. **Left:** Quantitative Gd distribution obtained by LA-ICP-MS/MS with a spatial resolution of 50 µm. Three regions of interest are designated. Region (**a**) showed a distribution of hot spots in the sub cutis with concentrations exceeding 100 µg/g, (**b**) contains a blood vessel and (**c**) exhibits connective tissue in the deeper skin. **Right:** Corresponding microscopic image.

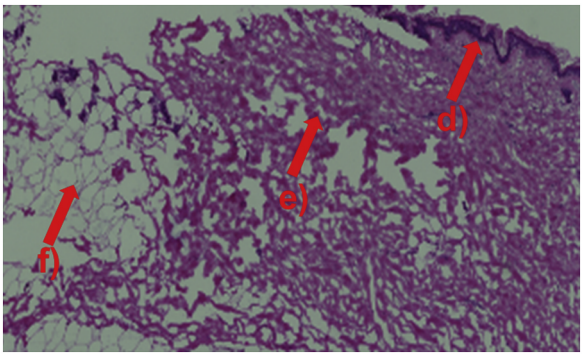

Fig. 3. H&E stained NSF skin of a consecutive tissue section (corresponding to region of interest (a), shown in Fig. 2). Different anatomical areas can be seen: epidermis (**d**), fatty tissue (**f**) and fibrotic tissue (**e**).

3.3. Brain tumour samples

Gd deposition in the brain was investigated in a brain biopsy originating from a patient with a glioblastoma tumour (IDH wildtype, grade IV WHO). Progression of glioblastoma is known to increase the permeability of the blood brain barrier due to localised damage. It was suspected that this patient's tumour burden would lead to detectable deposits of Gd following administration of Gd-HP-DO3A. Fig. 6 shows a 5 µm x 5 µm resolution image of the elemental distribution of the target elements in the brain tumour tissue. Like the deposits found in NSF skin tissue, the diameter was in the same range of approximately 50 µm x 50 µm or below. Correlations and co-localisation of Gd with P, Ca, Zn, as well as Fe were clearly evident. However, the Gd concentration in the tumour sample was a factor of 25–100 times lower than in the skin biopsies. The concentration of Gd in the deposits exceeded 1 µg/g in some instances, whilst other accumulations had lower concentrations between 0.2 µg/g and 0.6 µg/g.

These results are in agreement with findings from Xia et al., who reported Gd deposits smaller than 50 µm inside brain tumours using SEM/EDX, and similar correlations with other elements [7]. Smaller deposits were reported in diseased brain tissue by McDonald et al. [23].

Fig. 7 presents a zoom view of the quantitative Gd distribution as well as an overlay of the P distribution and the Gd distribution. Both distributions correlated in terms of shape, dimensions and locations. These findings support preceding studies that reported the formation of insoluble deposits containing P, Ca, Fe and Zn. While such deposits in the brain seem to have very similar elemental composition as those observed in the skin of NSF patients, the observed concentration in the brain were significantly lower than determined in NSF skin tissue.

4. Conclusion

The newly developed method was suitable for the determination of various elements that are important for the investigation of Gd retention in patients who have undergone MRI diagnostics after administration of Gd-based contrast agents. Tandem mass spectrometry resulted in superior detection limits for Gd, P, Fe, Zn, and Ca when compared against a standard SQ based method for EBI. The improved detection tune was suitable for investigation of Gd depositions in NSF skin and brain tissues at high spatial resolution (5µm x 5 µm). The Gd distribution was quantified employing matrix matched tissue standards

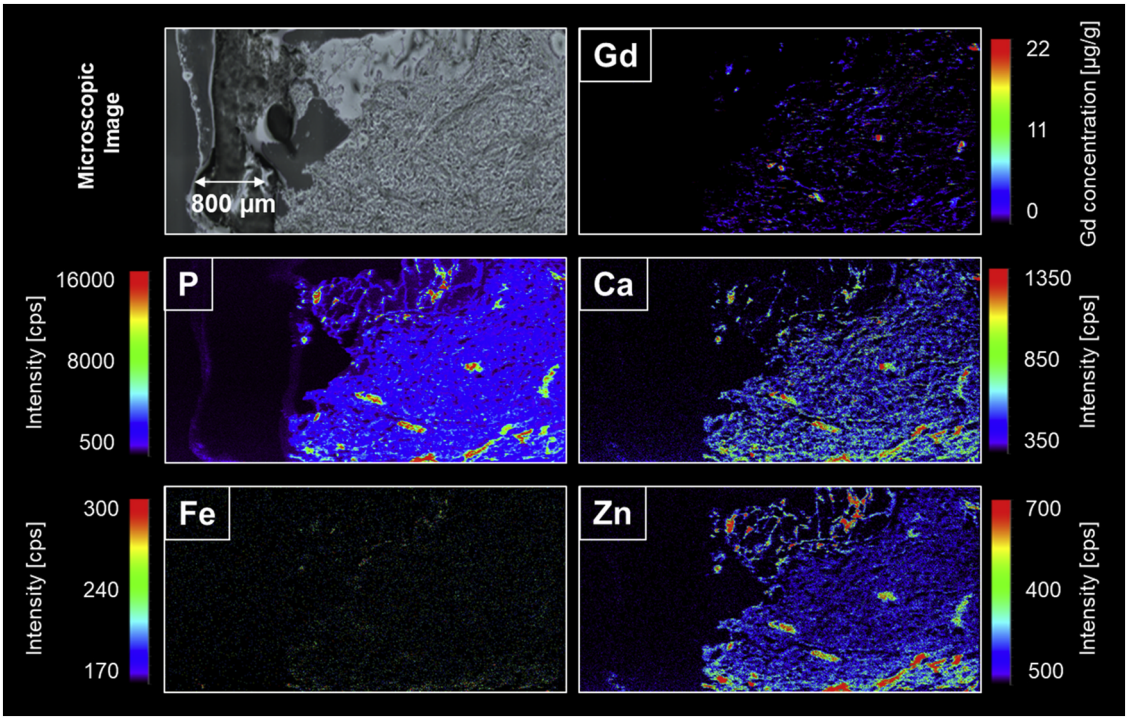

Fig. 4. A light microscopic image of NSF skin tissue (area a, Fig. 3) and the elemental distributions of Gd, P, Ca and Zn. Except for Fe, all elements show strong correlations.

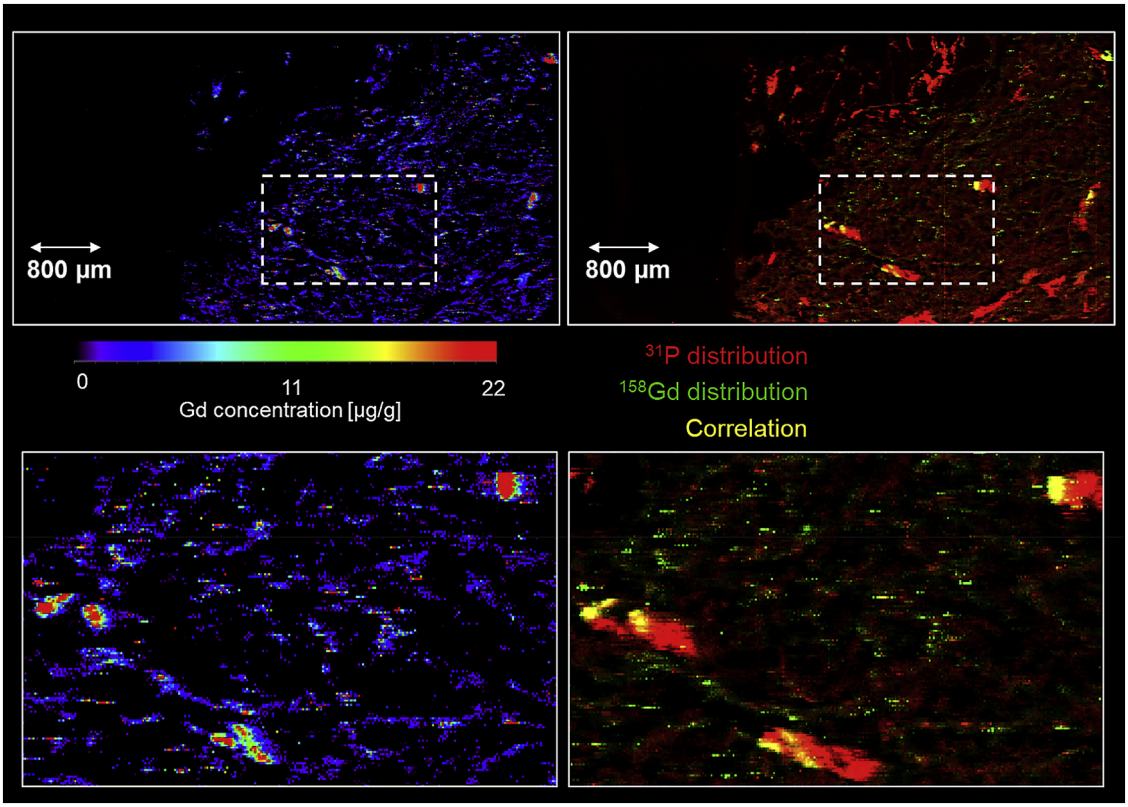

Fig. 5. The Gd distribution in NSF skin tissue is shown and correlated to the distribution of P. **Left:** Zoomed views of the Gd distribution. The deposits contained most of the Gd found in the tissue sample. The centre of the deposits exhibited highest concentrations exceeding 100 µg/g. **Right:** Overlay of the ^{31}P distribution (red) and the Gd distribution (green). Correlations are shown in yellow, showing smaller areas of Gd within P areas (For interpretation of the references to colour in this figure legend, the reader is referred to the web version of this article).

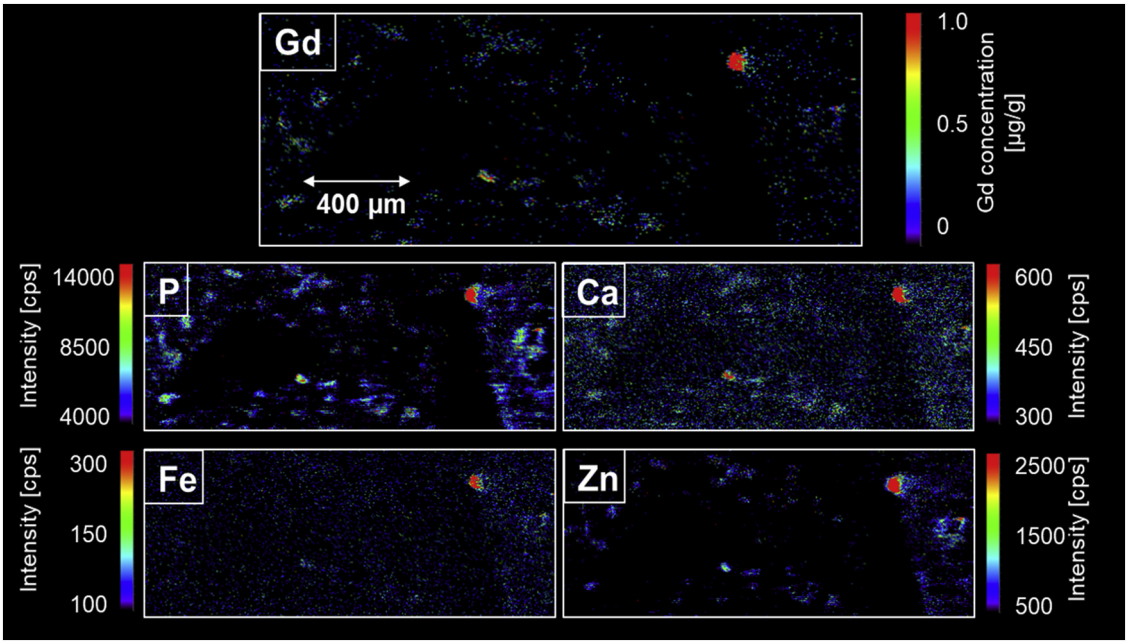

Fig. 6. Elemental distribution of Gd, P, Ca, Zn and Fe in a brain tissue section. The Gd distribution was calibrated using matrix-matched tissue standards.

enabling the calibration of small Gd deposits, also observed in other studies, with diameters of approximately 50 µm for the first time. The analysis furthermore allowed the high spatial resolution of P, Zn, Ca and Fe and enabled the identification of correlations. The results support the hypothesis that Gd is liberated in a transmetallation process and precipitated as an insoluble phosphate salt. This method is a viable tool for analyses requiring higher resolutions or lower detection limits of elements taking part in the pathogenesis of NSF and the deposition of Gd in brain tissue.

Conflict of interest statement

All authors declare that there is no conflict of interest associated with this manuscript.

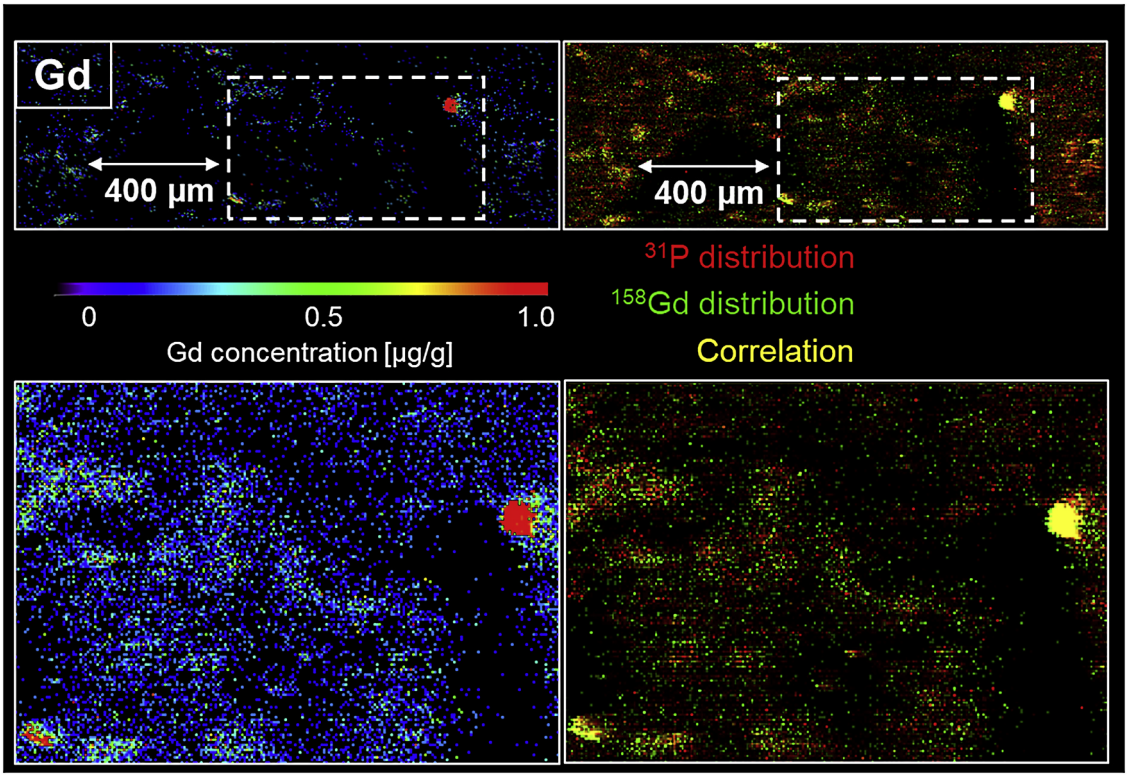

Fig. 7. Correlation of the Gd and P distribution in brain tissue. **Left:** Zoom view of the Gd distribution. The deposits contained most of the Gd in the brain tissue sample. The centre of the deposits exhibited highest concentrations exceeding 1 µg/g. **Right:** Overlay of the P distribution (red) and the Gd distribution (green). Correlations are shown in yellow showing a uniform distribution of P and ^{158}Gd within the deposits (For interpretation of the references to colour in this figure legend, the reader is referred to the web version of this article).

Acknowledgments

Images were analysed and created using imaging software by Robin Schmid (University of Muenster). DC is supported by an UA-DAAD collaboration grant. PAD is the recipient of an Australian Research Council Discovery Project (DP170100036).

References

[1] T. Grobner, Gadolinium - a specific trigger for the development of nephrogenic fibrosing dermopathy and nephrogenic systemic fibrosis? Nephrol. Dial. Transplant. 21 (2006) 1104–1108, https://doi.org/10.1093/ndt/gfk062.
[2] S.E. Cowper, H.S. Robin, S.M. Steinberg, L.D. Su, S. Gupta, P.E. LeBoit, Scleromyxoedema-like cutaneous diseases in renal-dialysis patients, Lancet 356 (2000) 1000–1001, https://doi.org/10.1016/S0140-6736(00)02694-5.
[3] P. Marckmann, L. Skov, K. Rossen, A. Dupont, M.B. Damholt, J.G. Heaf, H.S. Thomsen, Nephrogenic systemic fibrosis: suspected causative role of gadodiamide used for contrast-enhanced magnetic resonance imaging, J. Am. Soc. Nephrol. 17 (2006) 2359–2362.
[4] M. Birka, K.S. Wentker, E. Lusmöller, B. Arheilger, C.A. Wehe, M. Sperling, R. Stadler, U. Karst, Diagnosis of Nephrogenic Systemic Fibrosis by means of Elemental Bioimaging and Speciation Analysis, Anal. Chem. 87 (2015) 3321–3328, https://doi.org/10.1021/ac504488k.
[5] S. Swaminathan, W.A. High, J. Ranville, T.D. Horn, K. Hiatt, M. Thomas, H.H. Brown, S.V. Shah, Cardiac and vascular metal deposition with high mortality in nephrogenic systemic fibrosis, Kidney Int. 73 (2008) 1413–1418, https://doi.org/10.1038/ki.2008.76.
[6] S. Kasahara, Y. Miki, M. Kanagaki, A. Yamamoto, N. Mori, T. Sawada, T. Taoka, T. Okada, K. Togashi, Hyperintense dentate nucleus on unenhanced T1-weighted MR images is associated with a history of brain irradiation, Radiology 258 (2011) 222–228, https://doi.org/10.1148/radiol.10100508.
[7] D. Xia, R.L. Davis, J.A. Crawford, J.L. Abraham, Gadolinium released from MR contrast agents is deposited in brain tumors: in situ demonstration using scanning electron microscopy with energy dispersive X-ray spectroscopy, Acta Radiol. 51 (2010) 1126–1136, https://doi.org/10.3109/02841851.2010.515614.
[8] FDA Drug Safety Communication, FDA evaluating the risk of brain deposits with repeated use of gadolinium-based contrast agents for magnetic resonance imaging (MRI), (2015).
[9] D. Clases, M. Sperling, U. Karst, Analysis of metal-based contrast agents in medicine and the environment, TrAC- Trends Anal. Chem. 104 (2018) 135–147, https://doi.org/10.1016/j.trac.2017.12.011.
[10] Y. Cao, D.Q. Huang, G. Shih, M.R. Prince, Signal change in the dentate nucleus on T1-weighted MR images after multiple administrations of gadopentetate dimeglumine versus gadobutrol, Am. J. Roentgenol. 206 (2016) 414–419, https://doi.org/10.2214/AJR.15.15327.
[11] N. Murata, L.F. Gonzalez-Cuyar, K. Murata, C. Fligner, R. Dills, D. Hippe, K.R. Maravilla, Macrocyclic and other non–group 1 gadolinium contrast agents deposit low levels of gadolinium in brain and bone tissue, Invest. Radiol. 51 (2016) 447–453, https://doi.org/10.1097/RLI.0000000000000252.
[12] A.P. Kartamihardja, T. Nakajima, S. Kameo, H. Koyama, Y. Tsushima, Impact of impaired renal function on gadolinium retention after administration of gadolinium-based contrast agents in a mouse model, Invest. Radiol. 51 (2016) 655–660, https://doi.org/10.1097/RLI.0000000000000295.
[13] T.F. Flood, N.V. Stence, J.A. Maloney, D.M. Mirsky, Pediatric brain: repeated exposure to linear gadolinium-based contrast material is associated with increased signal intensity at unenhanced T1-weighted MR imaging, Radiology. 282 (2016) 222–228, https://doi.org/10.1148/radiol.2016160356.
[14] M. Birka, J. Roscher, M. Holtkamp, M. Sperling, U. Karst, Investigating the stability of gadolinium based contrast agents towards UV radiation, Water Res. 91 (2016) 244–250, https://doi.org/10.1016/j.watres.2016.01.012.
[15] D.R. Roberts, S.M. Lindhorst, C.T. Welsh, K.R. Maravilla, M.N. Herring, A.K. Braun, B.H. Thiers, W.C. Davis, High levels of gadolinium deposition in the skin of a patient with normal renal function, Invest. Radiol. 51 (2016) 280–289, https://doi.org/10.1097/RLI.0000000000000266.
[16] S. Fingerhut, A.-C. Niehoff, M. Sperling, A. Jeibmann, W. Paulus, T. Niederstadt, T. Allkemper, W. Heindel, M. Holling, U. Karst, Spatially resolved quantification of gadolinium deposited in the brain of a patient treated with gadolinium-based contrast agents, J. Trace Elem. Med. Biol. 45 (2018) 125–130, https://doi.org/10.1016/j.jtemb.2017.10.004.
[17] S. Fingerhut, M. Sperling, M. Holling, T. Niederstadt, T. Allkemper, A. Radbruch, W. Heindel, W. Paulus, A. Jeibmann, U. Karst, Gadolinium-based contrast agents induce gadolinium deposits in cerebral vessel walls, while the neuropil is not affected: an autopsy study, Acta Neuropathol. 136 (2018) 127–138, https://doi.org/10.1007/s00401-018-1857-4.
[18] S. Swaminathan, Gadolinium toxicity : Iron and ferroportin as central targets, Magn. Reson. Imaging 34 (2016) 1373–1376, https://doi.org/10.1016/j.mri.2016.08.016.
[19] C. Thakral, J.L. Abraham, Gadolinium-induced nephrogenic systemic fibrosis is associated with insoluble Gd deposits in tissues: In Vivo transmetallation confirmed by microanalysis, J. Cutan. Pathol. 36 (2009) 1244–1254, https://doi.org/10.1111/j.1600-0560.2009.01283.x.
[20] S.J. George, S.M. Webb, J.L. Abraham, S.P. Cramer, Synchrotron X-ray analyses demonstrate phosphate-bound gadolinium in skin in nephrogenic systemic fibrosis, Br. J. Dermatol. 163 (2010) 1077–1081, https://doi.org/10.1111/j.1365-2133.2010.09918.x.
[21] S.G. Schäd, P. Heitland, W.N. Kühn-Velten, G.E. Gross, L. Jonas, Time-dependent decrement of dermal gadolinium deposits and significant improvement of skin symptoms in a patient with nephrogenic systemic fibrosis after temporary renal failure, J. Cutan. Pathol. 40 (2013) 935–944, https://doi.org/10.1111/cup.12214.
[22] J.L. Abraham, S. Chandra, C. Thakral, J.M. Abraham, SIMS imaging of gadolinium isotopes in tissue from Nephrogenic Systemic Fibrosis patients: Release of free Gd from magnetic resonance imaging (MRI) contrast agents, Appl. Surf. Sci. 255 (2008) 1181–1184, https://doi.org/10.1016/j.apsusc.2008.05.140.
[23] R.J. McDonald, J.S. McDonald, D.F. Kallmes, M.E. Jentoft, D.L. Murray, K.R. Thielen, E.E. Williamson, L.J. Eckel, Intracranial gadolinium deposition after contrast-enhanced MR imaging, Radiology 275 (2015) 772–782, https://doi.org/10.1148/radiol.15150025.
[24] J.A. Schroeder, C. Weingart, B. Coras, I. Hausser, S. Reinhold, M. Mack, V. Seybold, T. Vogt, B. Banas, F. Hofstaedter, B.K. Krämer, Ultrastructural evidence of dermal gadolinium deposits in a patient with nephrogenic systemic fibrosis and end-stage renal disease, Clin. J. Am. Soc. Nephrol. 3 (2008) 968–975, https://doi.org/10.2215/CJN.00100108.
[25] C. Thakral, J. Alhariri, J.L. Abraham, Long-term retention of gadolinium in tissues from nephrogenic systemic fibrosis patient after multiple gadolinium-enhanced MRI scans: case report and implications, Contrast Media Mol. Imaging 2 (2007) 199–205, https://doi.org/10.1002/cmmi.146.
[26] J.L. Abraham, C. Thakral, L. Skov, K. Rossen, P. Marckmann, Dermal inorganic gadolinium concentrations: Evidence for in vivo transmetallation and long-term persistence in nephrogenic systemic fibrosis, Br. J. Dermatol. 158 (2008) 273–280, https://doi.org/10.1111/j.1365-2133.2007.08335.x.
[27] W.A. High, R.A. Ayers, J. Chandler, G. Zito, S.E. Cowper, Gadolinium is detectable within the tissue of patients with nephrogenic systemic fibrosis, J. Am. Acad. Dermatol. 56 (2007) 21–26, https://doi.org/10.1016/j.jaad.2006.10.047.
[28] R.C. Semelka, M. Ramalho, M. AlObaidy, J. Ramalho, Gadolinium in humans: a family of disorders, Am. J. Roentgenol. 207 (2016) 229–233, https://doi.org/10.2214/AJR.15.15842.
[29] D.P. Bishop, D. Clases, F. Fryer, E. Williams, S. Wilkins, D.J. Hare, N. Cole, U. Karst, P.A. Doble, Elemental bio-imaging using laser ablation-triple quadrupole-ICP-MS, J. Anal. At. Spectrom. 31 (2016) 197–202, https://doi.org/10.1039/c5ja00293a http://www.scopus.com/inward/record.url?eid=2-s2.0-84952894964&partnerID=tZOtx3y1.
[30] L. Balcaen, E. Bolea-Fernandez, M. Resano, F. Vanhaecke, Inductively coupled plasma – tandem mass spectrometry (ICP-MS/MS): a powerful and universal tool for the interference-free determination of (ultra)trace elements – a tutorial review, Anal. Chim. Acta 894 (2015) 7–19, https://doi.org/10.1016/j.aca.2015.08.053.
[31] E. Bolea-Fernandez, L. Balcaen, M. Resano, F. Vanhaecke, Overcoming spectral overlap via inductively coupled plasma-tandem mass spectrometry (ICP-MS/MS). A tutorial review, J. Anal. At. Spectrom. 32 (2017) 1660–1679, https://doi.org/10.1039/C7JA00010C.
[32] D.J. Hare, J. Lear, D. Bishop, A. Beavis, P.A. Doble, Protocol for production of matrix-matched brain tissue standards for imaging by laser ablation-inductively coupled plasma-mass spectrometry, Anal. Methods 5 (2013) 1915–1921, https://doi.org/10.1039/c3ay26248k.
[33] J. Lear, D.J. Hare, F. Fryer, P.A. Adlard, D.I. Finkelstein, P.A. Doble, High-resolution elemental bioimaging of Ca, Mn, Fe, Co, Cu, and Zn employing LA-ICP-MS and hydrogen reaction gas, Anal. Chem. 84 (2012) 6707–6714, https://doi.org/10.1021/ac301156f.